Recent Developments in Endmember Extraction and Spectral Unmixing

Antonio Plaza, Gabriel Martín, Javier Plaza, Maciel Zortea and Sergio Sánchez

Abstract Spectral unmixing is an important task for remotely sensed hyperspectral data exploitation. The spectral signatures collected in natural environments are invariably a mixture of the pure signatures of the various materials found within the spatial extent of the ground instantaneous field view of the imaging instrument. Spectral unmixing aims at inferring such pure spectral signatures, called *endmembers*, and the material fractions, called *fractional abundances*, at each pixel of the scene. In this chapter, we provide an overview of existing techniques for spectral unmixing and endmember extraction, with particular attention paid to recent advances in the field such as the incorporation of spatial information into the endmember searching process, or the use of nonlinear mixture models for fractional abundance characterization. In order to substantiate the methods presented throughout the chapter, highly representative hyperspectral scenes obtained by different imaging spectrometers are used to provide a quantitative and comparative algorithm assessment. To address the computational requirements introduced by hyperspectral imaging algorithms, the chapter also

A. Plaza (✉), G. Martín, J. Plaza and S. Sánchez
Department of Technology of Computers and Communications, University of
Extremadura, Avda. de la Universidad s/n, 10071 Caceres, Spain
e-mail: aplaza@unex.es

G. Martín
e-mail: gamahefpi@unex.es

J. Plaza
e-mail: jplaza@unex.es

S. Sánchez
e-mail: sersanmar@unex.es

M. Zortea
Department of Mathematics and Statistics, University of Tromso, 9037 Tromso, Norway
e-mail: maciel.zortea@hyperinet.eu

includes a parallel processing example in which the performance of a spectral unmixing chain (made up of spatial–spectral endmember extraction followed by linear spectral unmixing) is accelerated by taking advantage of a low-cost commodity graphics co-processor (GPU). Combined, these parts are intended to provide a snapshot of recent developments in endmember extraction and spectral unmixing, and also to offer a thoughtful perspective on future potentials and emerging challenges in designing and implementing efficient hyperspectral imaging algorithms.

Keywords Hyperspectral imaging · Spectral unmixing · Endmember extraction · Neural networks · Intelligent training · Parallel processing · GPUs

1 Introduction

Spectral mixture analysis (also called *spectral unmixing*) has been an alluring exploitation goal from the earliest days of hyperspectral imaging [1] to our days [2, 3]. No matter the spatial resolution, the spectral signatures collected in natural environments are invariably a mixture of the signatures of the various materials found within the spatial extent of the ground instantaneous field view of the imaging instrument [4]. For instance, it is likely that the pixel collected over a vegetation area in Fig. 1 actually comprises a mixture of vegetation and soil. In this case, the measured spectrum may be decomposed into a combination of pure spectral signatures of soil and vegetation, weighted by areal coefficients that indicate the proportion of each *macroscopically* pure signature in the mixed pixel [5].
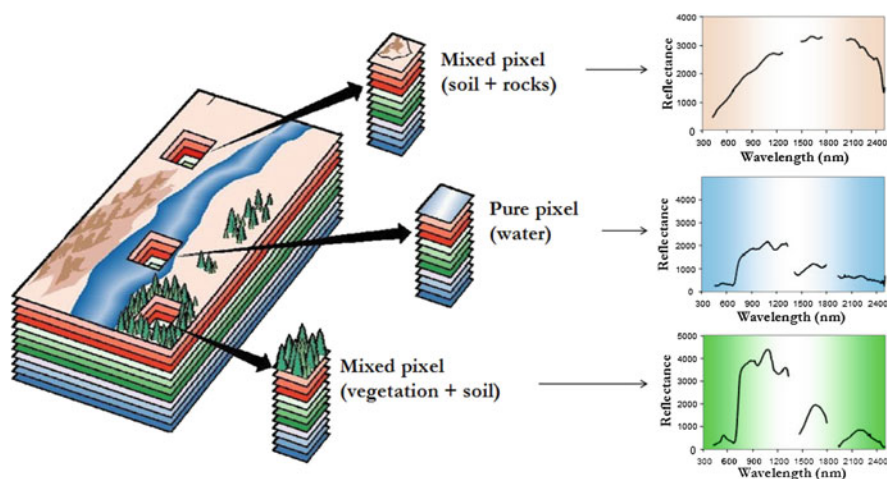
Fig. 1 The mixture problem in remotely sensed hyperspectral data analysis
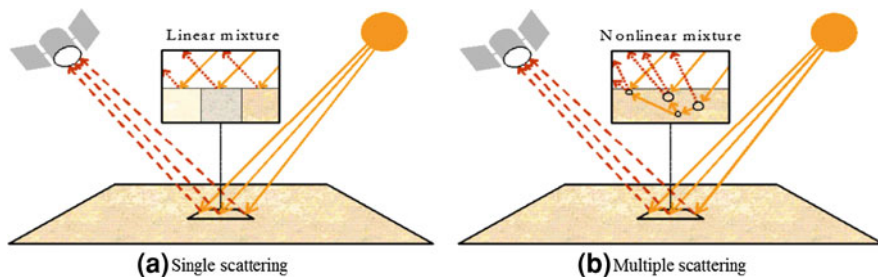
Fig. 2 Linear versus nonlinear mixture models: single versus multiple scattering

The availability of hyperspectral imagers with a number of spectral bands that exceeds the number of spectral mixture components [6] has allowed to cast the unmixing problem in terms of an over-determined system of equations in which, given a set of pure spectral signatures (called *endmembers*) the actual unmixing to determine apparent pixel *abundance fractions* can be defined in terms of a numerical inversion process [7].

A standard technique for spectral mixture analysis is *linear* spectral unmixing [8, 9], which assumes that the collected spectra at the spectrometer can be expressed in the form of a linear combination of endmembers weighted by their corresponding abundances. It should be noted that the linear mixture model assumes minimal secondary reflections and/or multiple scattering effects in the data collection procedure, and hence the measured spectra can be expressed as a linear combination of the spectral signatures of materials present in the mixed pixel (see Fig. 2a). Although the linear model has practical advantages such as ease of implementation and flexibility in different applications [10], *nonlinear* spectral unmixing may best characterize the resultant mixed spectra for certain endmember distributions, such as those in which the endmember components are randomly distributed throughout the field of view of the instrument [11, 12]. In those cases, the mixed spectra collected at the imaging instrument is better described by assuming that part of the source radiation is multiply scattered before being collected at the sensor (see Fig. 2b).

In this chapter, we provide an overview of existing techniques for spectral unmixing and endmember extraction, covering advances in both the linear and nonlinear mixture model, and with particular attention paid to recent advances in the field. The chapter is organized as follows. In Sect. 2, the chapter first focuses on the linear mixture model, introducing the formulation of the mixture problem under this model and further describing several classic approaches for endmember extraction (using different concepts) and linear spectral unmixing models (unconstrained, partially constrained and fully constrained). This section also covers recent developments in the linear mixture model by means of the incorporation of spatial information into the process of automatically extracting spectral endmembers from the image data, and further analyzes the impact of spatial information in the subsequent unmixing process. Section 3 addresses the nonlinear

mixture model by means of neural network-based techniques aimed at learning the complexity of nonlinear mixtures by means of automatic training sample selection algorithms which are used in the framework of a supervised learning procedure to characterize other mixed signatures in the input data. Section 4 presents a quantitative and comparative assessment of the different techniques for spectral unmixing presented in this chapter (linear and nonlinear), using hyperspectral data sets obtained by different instruments, such as the Airborne Visible Infra-Red Imaging Spectrometer (AVIRIS), operated by NASA/JPL, and the Digital Airborne (DAIS 7915) and Reflective Optics System (ROSIS) imaging spectrometers, operated by DLR in Germany. Section 5 presents an implementation case study in which a spectral unmixing chain made up of a spatial–spectral endmember extraction algorithm followed by a linear (unconstrained) fractional abundance estimation technique are implemented in parallel using commodity graphics processing units (GPU). Finally, Sect. 6 concludes with some remarks and hints at plausible future research avenues.

2 Linear Spectral Unmixing

2.1 Problem Formulation

Let us assume that a remotely sensed hyperspectral scene with n bands is denoted by $\mathbf{I}$, in which the pixel at the discrete spatial coordinates (i, j) of the scene is represented by a vector $\mathbf{X}(i,j) = [x_1(i,j), x_2(i,j), \ldots, x_n(i,j)] \in \Re^n$, where $\Re$ denotes the set of real numbers in which the pixel's spectral response $x_k(i, j)$ at sensor channels $k = 1, \ldots, n$ is included. Under the linear mixture model assumption, each pixel vector in the original scene can be modeled using the following expression:

$$\mathbf{X}(i,j) = \sum_{z=1}^{p} \Phi_z(i,j) \cdot \mathbf{E}_z + \mathbf{n}(i,j), \tag{1}$$

where $\mathbf{E}_z$ denotes the spectral response of endmember z, $\Phi_z(i, j)$ is a scalar value designating the fractional abundance of the endmember z at the pixel $\mathbf{X}(i, j)$, p is the total number of endmembers, and $\mathbf{n}(i, j)$ is a noise vector. Two physical constrains are generally imposed into the model described in (1), these are the abundance non-negativity constraint (ANC), i.e., $\Phi_z(i,j) \geq 0$, and the abundance sum-to-one constraint (ASC), i.e., $\sum_{z=1}^{p} \Phi_z(i,j) = 1$ [8]. The solution of the fully constrained linear spectral mixture problem described in (1) relies on two major requirements:

1. A successful estimation of how many endmembers, p, are present in the input hyperspectral scene $\mathbf{I}$, and

2. The correct determination of a set $\mathbf{E} = \{\mathbf{E}_z\}_{z=1}^p$ of endmembers and their correspondent abundance fractions $\Phi(i, j) = \{\Phi_z(i, j)\}_{z=1}^p$ at each pixel $\mathbf{X}(i, j)$.

In order to address the first requirement, a successful technique in the literature has been the virtual dimensionality (VD) [13]. The VD concept formulates the issue of whether a distinct signature is present or not in each of the spectral bands as a binary hypothesis testing problem, where a so-called Neyman-Pearson detector is generated to serve as a decision-maker based on a prescribed P_F (i.e., false alarm probability). In light of this interpretation, the issue of determining an appropriate value for p is further simplified and reduced to setting a specific value of P_F. As will be shown in experiments, a suitable empirical choice is $P_F = 10^{-3}$ or $P_F = 10^{-4}$, where the method used in this work to estimate the VD is the one developed by Harsanyi, Farrand and Chang [13] (referred to as HFC method) later modified by including a noise whitening process as preprocessing to remove the second-order statistical correlation. The purpose is that signal sources can be decorrelated from the noise to achieve better signal detection. The resulting method will be referred to as the noise-whitened HFC (NWHFC). The second requirement for successful implementation of the linear mixture model (availability of endmember extraction and abundance estimation techniques) will be addressed in the following subsections.

2.2 Endmember Extraction

Over the last decade, several algorithms have been developed for automatic or semi-automatic extraction of spectral endmembers [9]. Classic techniques include the pixel purity index (PPI) [14], N-FINDR [15–17], iterative error analysis (IEA) [18], optical real-time adaptive spectral identification system (ORASIS) [19], convex cone analysis (CCA) [20], vertex component analysis (VCA) [21], and an orthogonal subspace projection (OSP) technique in [22]. Other advanced techniques for endmember extraction have been recently proposed [23–29], but none of them considers spatial adjacency. However, one of the distinguishing properties of hyperspectral data is the multivariate information coupled with a two-dimensional (pictorial) representation amenable to image interpretation. Subsequently, most endmember extraction algorithms listed above could benefit from an integrated framework in which both the spectral information and the spatial arrangement of pixel vectors are taken into account. An example of this situation is given in Fig. 3, in which a hyperspectral data cube collected over an urban area (high spatial correlation) is modified by randomly permuting the spatial coordinates (i, j) of the pixel vectors, thus removing the spatial correlation. In both scenes, the application of a spectral-based endmember extraction method would yield the same analysis results while it is clear that a spatial–spectral technique could incorporate the spatial information present in the original scene into the endmember searching process.

Fig. 3 Example illustrating the importance of spatial information in hyperspectral analysis
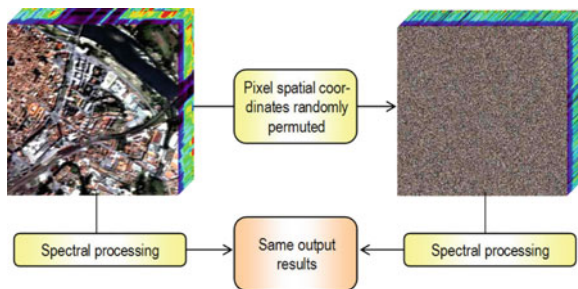

To the best of our knowledge, only a few attempts exist in the literature aimed at including the spatial information in the process of extracting spectral end-members. Extended morphological operations [30] have been used as a baseline to develop an automatic morphological endmember extraction (AMEE) algorithm [31] for spatial–spectral endmember extraction. Also, spatial averaging of spectrally similar endmember candidates found via singular value decomposition (SVD) was used in the development of the spatial spectral endmember extraction (SSEE) algorithm [32]. Recently, a spatial preprocessing (SPP) algorithm [33] has been proposed which estimates, for each pixel vector in the scene, a spatially derived factor that is used to weight the importance of the spectral information associated to each pixel in terms of its spatial context. The SPP is intended as a preprocessing module that can be used in combination with an existing spectral-based endmember extraction algorithm.

In the following, we describe in more detail three selected spectral-based algorithms (N-FINDR, OSP, VCA) and three spatial–spectral endmember extraction algorithms (AMEE, SSEE, SPP) that will be used in our comparison in this chapter. The reasons for our selection are: (1) these algorithms are representative of the class of convex geometry-based and spatial processing-based techniques which have been successful in endmember extraction; (2) they are fully automated; (3) they always produce the same final results for the same input parameters (for the N-FINDR, there is a random initialization step that also conditions the final output); and (4) the number of endmembers to be extracted, p, is an input parameter for all algorithms, while the AMEE, SSE and SPP have additional input parameters related with the definition of spatial context around each pixel in the scene.

2.2.1 N-FINDR

This algorithm looks for the set of pixels with the largest possible volume by *inflating* a simplex inside the data. The procedure begins with a random initial selection of pixels (see Fig. 4a). Every pixel in the image must be evaluated in order to refine the estimate of endmembers, looking for the set of pixels that maximizes the volume of the simplex defined by selected endmembers.

(a) N-FINDR initialized randomly ($p = 4$)   **(b)** Final volume estimation by N-FINDR
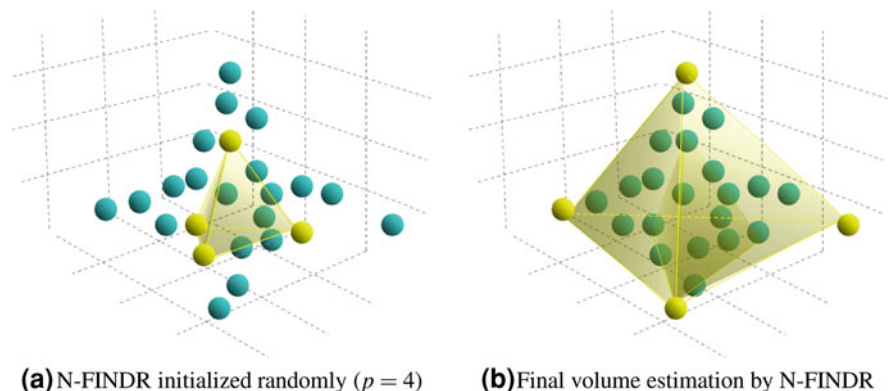
Fig. 4 Graphical interpretation of the N-FINDR algorithm in a three-dimensional space. **a** N-FINDR initialized randomly (p=4); **b** final volume estimation by N-FINDR

The corresponding volume is calculated for every pixel in each endmember position by replacing that endmember and finding the resulting volume. If the replacement results in a an increase of volume, the pixel replaces the endmember. This procedure is repeated until there are no more endmember replacements (see Fig. 4b). The mathematical definition of the volume of a simplex formed by a set of endmember candidates is proportional to the determinant of the set augmented by a row of ones. The determinant is only defined in the case where the number of features is $p - 1$, p being the number of desired endmembers [34]. Since in hyperspectral data typically $n \gg p$, a transformation that reduces the dimensionality of the input data, is required. In this study, the principal component transform (PCT) has been used [35, 36], although another widely used alternative that decorrelates the noise in the data is the maximum noise fraction (MNF) [37]. As a final comment, it has been observed that different random initializations of N-FINDR may produce different final solutions. Thus, our N-FINDR algorithm was implemented in iterative fashion, so that each sequential run was initialized with the previous algorithm solution, until the algorithm converges to a simplex volume that cannot be further maximized. Our experiments show that, in practice, this approach allows the algorithm to converge in a few iterations only.

2.2.2 Orthogonal Subspace Projection (OSP)

This algorithm starts by selecting the pixel vector with maximum length in the scene as the first endmember. Then, it looks for the pixel vector with the maximum absolute projection in the space orthogonal to the space linearly spanned by the initial pixel, and labels that pixel as the second endmember. A third endmember is found by applying an orthogonal subspace projector to the original image [22], where the signature that has the maximum orthogonal projection in the space

orthogonal to the space linearly spanned by the first two endmembers. This procedure is repeated until the desired number of endmembers, p, is found [38].

### 2.2.3 Vertex Component Analysis (VCA)

This algorithm also makes use of the concept of orthogonal subspace projections. However, as opposed to the OSP algorithm described above, the VCA exploits the fact that the endmembers are the vertices of a simplex, and that the affine transformation of a simplex is also a simplex [21]. As a result, VCA models the data using a positive cone, whose projection onto a properly chosen hyperplane is another simplex whose vertices are the final endmembers. After projecting the data onto the selected hyperplane, the VCA projects all image pixels to a random direction and uses the pixel with the largest projection as the first endmember. The other endmembers are identified in sequence by iteratively projecting the data onto a direction orthogonal to the subspace spanned by the endmembers already determined. The new endmember is then selected as the pixel corresponding to the extreme projection, and the procedure is repeated until a set of p endmembers is found [21]. In our experiments with VCA, we select the corresponding pixel original spectra as the VCA solution, not the noise-smoothed solution produced by the original algorithm. In practice, our approach is expected to slightly reduce the performance of VCA for low signal-to-noise (SNR) ratios, but we also believe that this decision allows a fair comparison of VCA to N-FINDR and OSP, which do not incorporate such noise reduction stage.

2.2.4 Automatic Morphological Endmember Extraction (AMEE)

The automatic morphological endmember extraction (AMEE) [31] algorithm runs on the full data cube with no dimensional reduction, and begins by searching spatial neighborhoods around each pixel vector $\mathbf{X}(i, j)$ in the image for the most spectrally pure and mostly highly mixed pixel. This task is performed by using extended mathematical morphology operators [30] of dilation and erosion, which are graphically illustrated on Fig. 5. Here, dilation selects the most spectrally pure pixel in a local neighborhood around each pixel vector $\mathbf{X}(i, j)$, while erosion selects the most highly mixed pixel in the same neighborhood. Each spectrally pure pixel is then assigned an *eccentricity* value, which is calculated as the spectral angle distance (SAD) [5, 10] between the most spectrally pure and mostly highly mixed pixel for each given spatial neighborhood. This process is repeated iteratively for larger spatial neighborhoods up to a maximum size that is predetermined. At each iteration the eccentricity values of the selected pixels are updated. The final endmember set is obtained by applying a threshold to the resulting greyscale eccentricity image, which results in a large set of endmember candidates. The final endmembers are extracted after applying the OSP method to
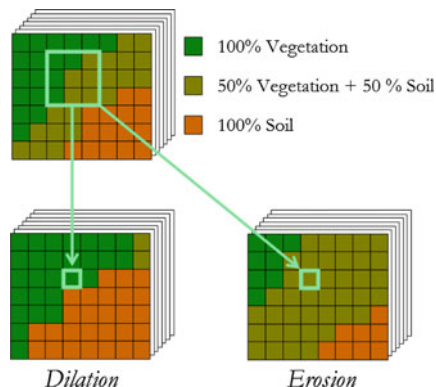
the set of candidates in order to derive a final set of spectrally distinct endmembers $\{\ \mathbf{E}_z\ \}_{z=1}^{p}$, where p is an input parameter to the OSP algorithm.

### 2.2.5 Spatial Spectral Endmember Extraction (SSEE)

The spatial–spectral endmember extraction tool (SSEE) uses spatial constraints to improve the relative spectral contrast of endmember spectra that have minimal unique spectral information, thus improving the potential for these subtle, yet potentially important endmembers, to be selected. With SSEE, the spatial characteristics of image pixels are used to increase the relative spectral contrast between spectrally similar, but spatially independent endmembers. The SSEE algorithm searches an image with a local search window centered around each pixel vector $\mathbf{X}(i, j)$ and comprises four steps [32]. First, the singular value decomposition (SVD) transform is applied to determine a set of eigenvectors that describe most of the spectral variance in the window or partition (see Fig. 6). Second, the entire image data are projected onto the previously extracted eigenvectors to determine a set of candidate endmember pixels (see Fig. 7).
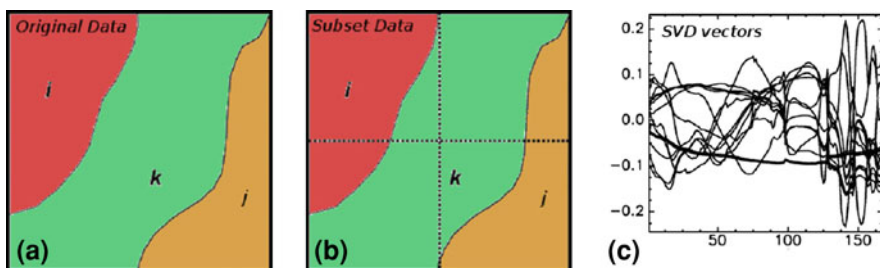
Fig. 6 First step of the SSEE algorithm. **a** Original data. **b** Subset data after spatial partitioning. **c** Set of representative SVD vectors used to describe spectral variance. This scene is reproduced from the one originally presented in [32]
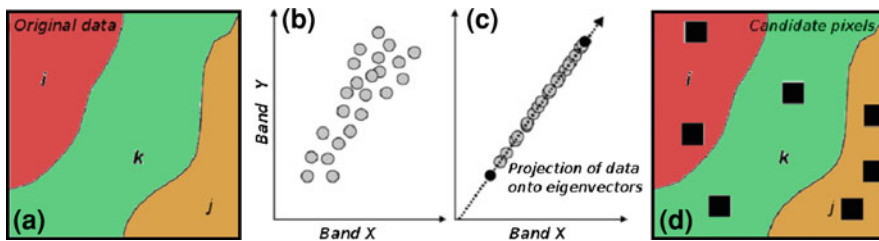
Fig. 7 Second step of the SSEE algorithm. **a** Original data. **b** Spectral distribution in two-dimensional space. **c** Projection of data onto eigenvectors. **d** Set of candidate pixels. This scene is reproduced from the one originally presented in [32]
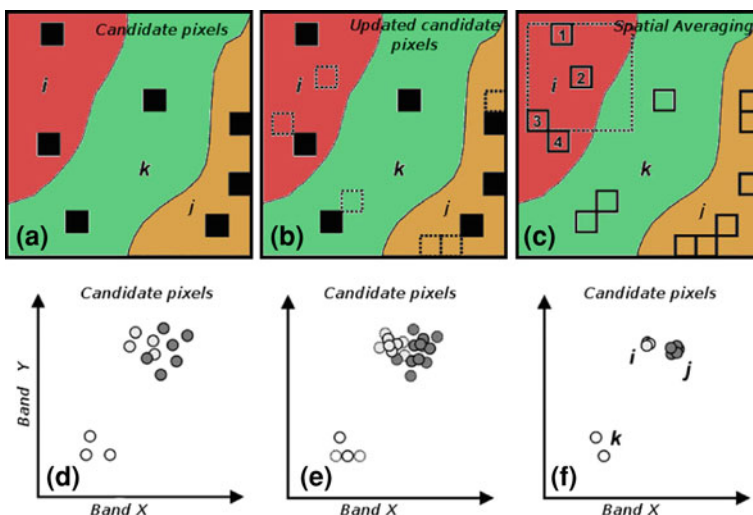
Fig. 8 Third step of the SSEE algorithm. **a** Set of candidate pixels. **b** Updated candidate pixels after including pixels which are spectrally similar to those in the original set. **c** Spatial averaging process of candidate endmember pixels using a sliding window centered on each candidate. **d** First iteration of spatial–spectral averaging. Averaged pixels shown as thick lines, with original pixels shown as thinner lines. **e** Second iteration of spatial–spectral averaging. **f** Continued iterations compress endmembers into clusters with negligible variance. This scene is reproduced from the one originally presented in [32]

Then, spatial constraints are used to combine and average spectrally similar candidate endmember pixels by testing, for each candidate pixel vector, which other pixel vectors are sufficiently similar in spectral sense (see Fig. 8). Instead of using a manual procedure as recommended by the authors in [32], we have used the OSP technique in order to derive a final set of spectrally distinct endmembers $\{\mathbf{E}_z\}_{z=1}^{p}$, where p is an input parameter to the OSP algorithm.

2.2.6 Spatial Pre-Processing (SPP)

The SPP [33] serves as a preprocessing module which can be combined with existing spectral-based algorithms such as the N-FINDR, OSP and VCA. The method estimates, for each input pixel vector, a scalar factor which is intimately related to the spatial similarity between the pixel and its spatial neighbors, and then uses this scalar factor to spatially weight the spectral information associated to the pixel. A simple geometric interpretation of the scalar factor is illustrated in Fig. 9, given as a toy example in which only two spectral bands of an input hyperspectral scene are represented against each other for visualization purposes. The idea behind the SPP is to center each spectral feature in the data cloud around its mean value, and then shift each feature straight towards the centroid of the data cloud (denoted by O′ in Fig. 9). The shift is proportional to a similarity measure calculated using both the spatial neighborhood around the pixel under consideration and the spectral information associated to the pixel, but without averaging the spectral signature of the pixel. The correction is performed so that pixels located in spatially homogenous areas (such as the pixel vector labeled as '1' in Fig. 9) are expected to have a smaller displacement with regards to their original location in the data cloud than pure pixels surrounded by spectrally distinct substances (e.g., the pixel vectors labeled as '2' and '3' in Fig. 9).

Resulting from the above operation, a modified simplex is formed, using not only spectral but also spatial information. It should be noted that the vertices of the modified simplex are more likely to be pure pixels located in spatially homogenous areas. Although the proposed method is expected to privilege homogeneous areas for the selection of endmembers, no pixel is excluded from the competitive

Fig. 9 Geometric interpretation of the SPP method for spatial preprocessing prior to endmember extraction. This scene is reproduced from the one originally presented in [33]
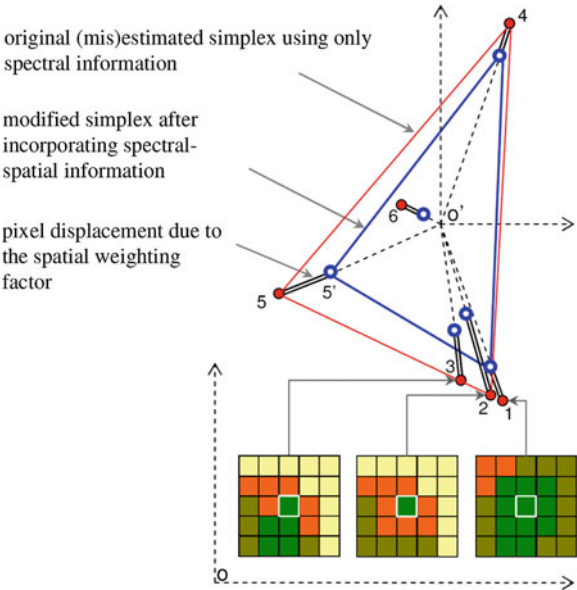
endmember extraction process that follows the preprocessing. As it can be inferred from Fig. 9, the proposed method is also expected to be robust in the presence of outliers. It is important to notice that the modified simplex in Fig. 9 is mainly intended to serve as a guide for a subsequent competitive endmember extraction process, conducted using a user-defined algorithm. However, such modified simplex is not intended to replace the simplex in the input hyperspectral scene. To achieve this, the spatial coordinates of the endmembers extracted from the preprocessed image are retained, but the spectral signatures associated to those spatial coordinates are obtained from the original hyperspectral scene.

2.3 Unconstrained Versus Constrained Linear Spectral Unmixing

Once a set of endmembers $\mathbf{E} = \{\mathbf{E}_z\}_{z=1}^{p}$ have been extracted, their correspondent abundance fractions $\Phi(i, j) = \{\Phi_z(i, j)\}_{z=1}^{p}$ in a specific pixel vector $\mathbf{X}(i, j)$ of the scene can be estimated (in least squares sense) by the following unconstrained expression [10]:

$$\hat{\Phi}_{\mathrm{UC}}(i,j) = (\mathbf{E}^T\mathbf{E})^{-1}\mathbf{E}^T\mathbf{X}(i,j). \tag{2}$$

However, it should be noted that the fractional abundance estimations obtained by means of Eq. 2 do not satisfy the ASC and ANC constraints. Imposing the ASC constraint results in the following optimization problem:

$$\min_{\Phi(i,j)\in\Delta}\left\{(\mathbf{X}(i,j) - \Phi(i,j)\cdot\mathbf{E})^T(\mathbf{X}(i,j) - \Phi(i,j)\cdot\mathbf{E})\right\},$$
$$\text{subject to: } \Delta = \left\{\Phi(i,j) \mid \sum_{z=1}^{p}\Phi_z(i,j) = 1\right\}. \tag{3}$$

Similarly, imposing the ANC constraint results in the following optimization problem:

$$\min_{\Phi(i,j)\in\Delta}\left\{(\mathbf{X}(i,j) - \Phi(i,j)\cdot\mathbf{E})^T(\mathbf{X}(i,j) - \Phi(i,j)\cdot\mathbf{E})\right\},$$
$$\text{subject to: } \Delta = \left\{\Phi(i,j) \mid \Phi_z(i,j) \geq 0 \text{ for all } 1 \leq z \leq p\right\}. \tag{4}$$

As indicated in [13], a non-negative constrained least squares (NCLS) algorithm can be used to obtain a solution to the ANC-constrained problem described in Eq. 4 in iterative fashion [39]. In order to take care of the ASC constraint, a new endmember signature matrix, denoted by $\mathbf{E}'$, and a modified version of the pixel vector $\mathbf{X}(i, j)$, denoted by $\mathbf{X}'(i, j)$, are introduced as follows:

$$\mathbf{E}' = \begin{bmatrix}\delta\mathbf{M}\\\mathbf{1}^T\end{bmatrix}, \Phi'(i,j) = \begin{bmatrix}\delta\Phi(i,j)\\1\end{bmatrix}, \tag{5}$$

where $\mathbf{1} = \underbrace{(1, 1, \ldots, 1)}_{p}^{T}$ and δ controls the impact of the ASC constraint. Using the two expressions in (5), a fully constrained estimate can be directly obtained from the NCLS algorithm by replacing $\mathbf{E}$ and $\Phi(i, j)$ used in the NCLS algorithm with $\mathbf{E}'$ and $\Phi'(i, j)$. Hereinafter, we will refer to the fully constrained (i.e. ASC-constrained and ANC-constrained) linear spectral unmixing model by the acronym FCLSU.

3 Nonlinear Spectral Unmixing

3.1 Problem Formulation

Under the nonlinear mixture model assumption, each pixel vector in the original scene can be modeled using the following expression:

$$\mathbf{X}(i, j) = f(\mathbf{E}, \Phi(i, j)) + \mathbf{n}(i, j), \tag{6}$$

where f is an unknown nonlinear function that defines the interaction between $\mathbf{E}$ and $\Phi(i, j)$. Various learning-from-data techniques have been proposed in the literature to estimate f. In particular, artificial neural networks have demonstrated great potential to decompose mixed pixels due to their inherent capacity to approximate complex functions [40]. Although many neural network architectures exist, for decomposition of mixed pixels in terms of nonlinear relationships mostly feed-forward networks of various layers, such as the multi-layer perceptron (MLP), have been used [12, 41, 42]. It has been shown in the literature that MLP-based neural models, when trained accordingly, generally outperform other non-linear models such as regression trees or fuzzy classifiers [43].

A variety of issues have been investigated in order to evaluate the impact of training in mixed pixel classification accuracy, including the size and location of training sites, and the composition of training sets, but most of the attention has been paid to the issue of training set size, i.e., the number of training samples required for the learning stage [44]. Sometimes the smallness of a training set represents a major problem [45]. This is especially apparent for analyses using hyperspectral sensor data, where the requirement of large volumes of training sites is a serious limitation [46]. Even if the endmembers participating in mixtures in a certain area are known, proportions of these endmembers on a per-pixel basis are difficult to be estimated a priori. Therefore, one of the most challenging aspects in the design of neural network-based techniques for spectral mixture analysis is to reduce the need for very large training sets. Studies have investigated a range of issues [47], including the use of feature selection and feature extraction methods to reduce the dimensionality of the input data [48], the use of unlabeled and semi-labeled samples [46], the accommodation of spatial dependence in the data to

define an efficient sampling design [32], or the use of statistics derived on other locations [49]. Our speculation is that the problem of mixed pixel interpretation demands intelligent training sample selection algorithms, able to seek for the most informative training samples, thus optimizing the compromise between estimation accuracy (to be maximized) and ground-truth knowledge (to be minimized).

A second issue that has not received attention in neural network-based mixed pixel analysis has to do with initial model conditions. For instance, the MLP neural network is typically trained using the error back-propagation algorithm [40]. It is a supervised technique of training with three phases. In the first one, an initial vector is presented to the network, which leads to the activation of the network as a whole. The second phase computes an error between the output vector and a vector of desired values for each output unit, and propagates it successively back through the network. The last phase computes the changes for the connection weights, which are randomly generated in the beginning. According to algorithm design, a good and effective learning algorithm should not depend on initial conditions, which can only affect the algorithm convergence rate, but should not alter the final results. The matter of fact is that this is generally not true in learning algorithms used for neural networks, where the choice of initial weights determines which minimum the algorithm will converge to [11]. In order for a mixture model to be effective, initial values must be representative and cannot be arbitrary.

In this section, we develop a combined linear/nonlinear mixture model which assumes that most of the mixed spectra in the data can be modeled via a combination of single and multiple scattering effects. The abundance fractions of endmember substances are first estimated via a linear mixture model and used to establish the initial condition, including the initial weight matrix. Such an initial estimation is then refined using an MLP neural network, coupled with unsupervised algorithms for intelligent selection of training samples from the available data. One of our main reasons to select an MLP neural network for demonstration is that this architecture has been often claimed to be sensitive to network architecture parameters, such as the arrangement and number of neurons in the different layers [41]. In our experience, however, a very simple MLP network configuration can produce stable results when initialized and trained accordingly, a fact that leads us to believe that both initialization and training can indeed be more important than the choice of a specific network architecture in mixture analysis applications.

3.2 Neural Network-Based Spectral Unmixing

Figure 10 shows a schematic block diagram of the proposed neural network-based unmixing architecture. The first step consists of an estimation of the number of endmembers, p, in the input data. For this purpose, in this work we use the VD concept [13]. Then, the model is initialized via a fully constrained linear mixture model based on automatic endmember extraction. Finally, the model is refined by
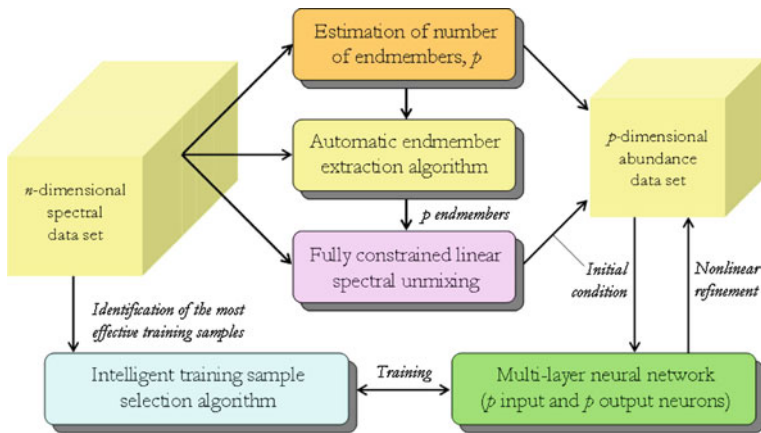
Fig. 10 Neural network-based spectral unmixing architecture

a supervised MLP neural network. The latter step is supported by an unsupervised algorithm for intelligent selection of training samples (both pure and mixed) from the data in order to estimate the final endmember fractional abundances. The number of neurons at the input layer of the MLP architecture equals the number of spectral endmembers found in the initialization stage. The input patterns to the input layer are vectors of endmember fractional abundances for each sample vector $\mathbf{X}(i, j)$, first estimated by FCLSU. The second layer is the hidden layer, and the third layer is the output layer. The number of neurons at the output layer, p, equals the number of estimated endmembers. It should be noted that the number of hidden neurons in the MLP architecture can be fine-tuned depending on the problem under consideration [40]. However, in this work we are mainly interested in exploring training mechanisms and their implications, without particular emphasis on careful adjustment of neural network configuration parameters. Subsequently, finding optimal parameters for the hidden layer is beyond our scope. Based on previous results in the literature and our own experimentation, we have considered one hidden layer only, with the number of neurons empirically set to the square root of the product of the number of input features and information classes, a configuration that has been shown to be successful for MLP-based mixed pixel characterization in previous work [43].

At this point, it is worth noting that most available neural models for multi-dimensional data analysis in the literature assume that the neuron count at the input layer equals the dimension of the input vectors, i.e., each neuron in the input layer is associated with one of the n spectral bands in which a pixel's reflectance spectrum is measured. However, the above configuration may easily suffer from limited training samples in hyperspectral analyses, where training data are often of limited quantity relative to input space dimensionality [36]. This leads any induced classifier to potentially feature a poor generalization capability, an effect known as the Hughes effect or *curse of the dimensionality*. Numerous analyses have been

undertaken founded on the desire to reduce the dimensionality of the input data prior to the analysis. In order to overcome the limitations above, in this work we adopt a simple, yet natural approach to represent an n-dimensional pixel vector as a p-dimensional vector of endmember fractional abundances at the pixel. This strategy allows for a reduction in the number of network connections without losing the information that is crucial for spectral unmixing applications. It should be noted that the issue of how to select the most informative training data (in terms of mixing knowledge) is of great importance for the success of the nonlinear learning stage. In the following subsection, we develop an unsupervised algorithm which selects training samples based on the mixture information they contain, thus allowing us to accommodate the information provided by mixed pixels into the learning process.

3.3 Automatic Selection and Labeling of Training Samples

The quality of training has a significant effect on mixed pixel characterization using neural networks [44]. Conventional approaches for selection of training samples often perform this task randomly, or by choosing the samples located in exemplar regions of each class only, while atypical cases are often removed or down-weighted in training set refinement operations. Such exemplar training patterns are located near the central *core* of the class in feature space. However, a key concern in the context of mixed pixel interpretation is how to identify and characterize the response of sites that lie away from the class core, and near to the decision boundaries commonly used in conventional, *pure* pixel classification. Therefore, *border* [47] (or, equivalently, *mixed*) training samples may be useful to refine a set of fractional abundance estimations obtained by using only spectrally pure training samples.

In this section, we describe a new technique for automatic selection and labeling of training samples from the input hyperspectral data. The proposed technique, called mixed training algorithm (MTA), first uses Winter's N-FINDR algorithm [15] as an approach to automatically label spectrally pure training samples (endmembers) without prior knowledge. Then, it iteratively seeks for the most highly mixed pixels in the input data set by following a procedure which behaves in an opposite way as N-FINDR and other convex geometry-based endmember extraction methods [9], i.e. it automatically selects and labels highly mixed training samples. Different sets of training samples, obtained by the MTA discussed in this section, will be used in the following section to investigate the impact of the composition of the training set on the characterization of mixed pixels. The MTA can be summarized by the following steps:

1. Compute $\mathbf{C}_p = (1/p) \sum_{z=1}^{p} \mathbf{E}_z$, i.e., the centroid of the simplex defined by the set of spectral endmembers $\mathbf{E} = \{\mathbf{E}_z\}_{z=1}^{p}$ produced for the input hyperspectral scene by an endmember extraction algorithm such as N-FINDR.

2. At iteration $j \geq 1$, calculate a point-wise spectral *distance* between each pixel vector $\mathbf{X}(i, j)$ in the input hyperspectral data and $\mathbf{C}_p$, and mark the pixel vector which provides the lowest *distance* value (i.e., the most spectrally similar to $\mathbf{C}_p$) as a new training sample $\mathbf{T}_j$.
3. Remove the pixel previously selected as a training sample from the input hyperspectral scene and apply a spectral screening algorithm to identify the pixel vectors with associated spectral signatures within a small spectral angle θ from any of the previously selected training samples, removing those samples from the input data as well.
4. Repeat from step 2 until a final set of k mixed labeled training samples $\{\mathbf{T}_j\}_{j=1}^k$ is generated from the input hyperspectral scene.

It should be noted that the MTA algorithm was implemented using various spectral similarity measures [5, 10], such as the SAD or the spectral information divergence (SID). In all cases, the results obtained were very similar. As a result, this paper only reports experiments based on using SAD for demonstration purposes.

4 Experimental Results

In this section we present two experiments focused on evaluating the endmember extraction and spectral unmixing techniques discussed throughout the chapter. In our first experiment, we focus on a mineral mapping application and further discuss the role of endmember extraction and the use of spatial information for linear spectral unmixing purposes, using AVIRIS image data collected over the Cuprite mining district in Nevada. In our second experiment, we provide a comparison of linear versus nonlinear spectral unmixing techniques in the context of a real agriculture and farming application in the region of Extremadura, Spain, using hyperspectral data sets collected by the DAIS 7915 and the ROSIS imaging spectrometers operating simultaneously at multiple resolutions.

4.1 First Experiment: AVIRIS Hyperspectral Data

In this experiment we use the well-known AVIRIS Cuprite data set, available online in reflectance units[1] after atmospheric correction. This scene has been widely used to validate the performance of endmember extraction algorithms. The portion used in experiments corresponds to a 350 × 350-pixel subset of the sector labeled as f970619t01p02_r02_sc03.a.rfl in the online data. The scene (displayed in Fig. 11a) comprises 224 spectral bands between 0.4 and 2.5 μm, with full width

---

[1] http://aviris.jpl.nasa.gov/html/aviris.freedata.html
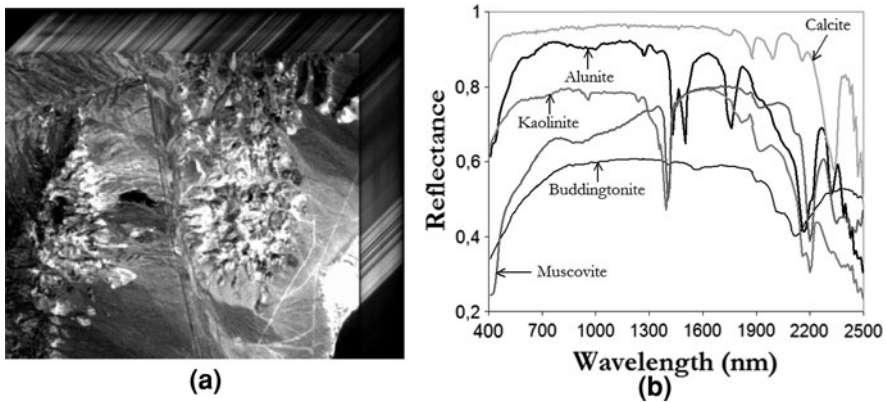
Fig. 11 **a** AVIRIS Cuprite data cube. **b** USGS spectral signatures of five representative minerals in the Cuprite mining district

at half maximum of 10 nm and spatial resolution of 20 m per pixel. Prior to the analysis, several bands were removed due to water absorption and low SNR in those bands, leaving a total of 192 reflectance channels to be used in the experiments. The Cuprite site is well understood mineralogically [50, 51], and has several exposed minerals of interest included in a spectral library compiled by the U.S. Geological Survey (USGS).[2] A few selected spectra from the USGS library, corresponding to several highly representative minerals in the Cuprite mining district (see Fig. 11b), are used in this work to substantiate endmember signature purity.

Two different metrics have been used to compare the performance of endmember extraction and spectral unmixing algorithms in the AVIRIS Cuprite scene. The first metric is the SAD between each extracted endmember and the set of available USGS ground-truth spectral signatures. For the sake of clarity, we remind that the SAD between two pixel vectors $\mathbf{X}(i, j)$ and $\mathbf{X}(r, s)$ can be simply defined as follows:

$$\text{SAD}(\mathbf{X}(i,j), \mathbf{X}(r,s)) = \cos^{-1} \frac{\mathbf{X}(i,j) \cdot \mathbf{X}(r,s)}{\|\mathbf{X}(i,j)\|\|\mathbf{X}(r,s)\|}. \tag{7}$$

It should be noted that SAD is given by the spectral angle formed by n-dimensional vectors (in radians). As a result, low SAD scores mean high spectral similarity between the compared vectors. This spectral similarity measure is invariant in the multiplication of $\mathbf{X}(i, j)$ and $\mathbf{X}(r, s)$ by constants and, consequently, is invariant before unknown multiplicative scalings that may arise due to differences in illumination and angular orientation [5]. The SAD metric allows us to identify the USGS signature which is most similar to each endmember automatically

---

[2] http://speclab.cr.usgs.gov/spectral-lib.htm

extracted from the scene by observing the minimum SAD distance reported for such endmember across the entire set of USGS signatures. The second metric is based on the assumption that a set of high-quality endmembers (and their corresponding FCLSU-estimated abundance fractions) may allow reconstruction of the original hyperspectral scene (by means of Eq. 1) with higher precision than a set of low-quality endmembers.

A second metric employed to evaluate the goodness of the reconstruction is the RMSE between the original and the reconstructed hyperspectral scene, which can be defined as follows. Let us assume that $\mathbf{I}^{(O)}$ is the original hyperspectral scene, and that $\mathbf{I}^{(R)}$ is a reconstructed version of $\mathbf{I}^{(O)}$, obtained using Eq. 1 with a set of endmembers, automatically derived by a certain algorithm from the original scene, and their corresponding FCLSU-estimated fractional abundances. Let us also assume that the pixel vector at spatial coordinates (i, j) in the original hyperspectral scene is given by $\mathbf{X}^{(O)}(i, j) = [x_1^{(O)}(i, j), x_2^{(O)}(i, j), ..., x_n^{(O)}(i, j)]$, while the corresponding pixel vector at the same spatial coordinates in the reconstructed hyperspectral scene is given by $\mathbf{X}^{(R)}(i, j) = [x_1^{(R)}(i, j), x_2^{(R)}(i, j), ..., x_n^{(R)}(i, j)]$. With the above notation in mind, the RMSE between the original and the reconstructed hyperspectral scenes is calculated as follows:

$$\text{RMSE}(\mathbf{I}^{(O)}, \mathbf{I}^{(R)}) = \frac{1}{s \times l} \sum_{i=1}^{s} \sum_{j=1}^{l} \left(\frac{1}{n} \sum_{k=1}^{n} [x_k^{(O)}(i,j) - x_k^{(R)}(i,j)]^2 \right)^{1/2}. \quad (8)$$

Table 1 tabulates the SAD scores (in degrees) obtained after comparing the USGS library spectra of five highly representative minerals in the Cuprite mining district (*alunite*, *buddingtonite*, *calcite*, *kaolinite* and *muscovite*) with the corresponding endmembers extracted by different algorithms from the AVIRIS Cuprite scene. In all cases, the input parameters of the different endmember extraction methods tested have been carefully optimized so that the best performance for each method is reported. The smaller the SAD values across the five minerals in Table 1, the better the results. It should be noted that Table 1 only displays the smallest SAD scores of all endmembers with respect to each USGS signature for each algorithm. For reference, the mean SAD values across all five USGS

Table 1 SAD-based spectral similarity scores (in degrees) between the USGS mineral spectra and their corresponding endmember pixels produced by several endmember extraction algorithms

Algorithm	Alunite	Buddigntonite	Calcite	Kaolinite	Muscovite	Mean
N-FINDR	9.96°	7.71°	12.08°	13.27°	5.24°	9.65°
OSP	4.81°	4.16°	9.62°	11.14°	5.41°	7.03°
VCA	10.73°	9.04°	6.36°	14.05°	5.41°	9.12°
AMEE	4.81°	4.21°	9.54°	8.74°	4.61°	6.38°
SSEE	4.81°	4.16°	8.48°	11.14°	4.62°	6.64°
SPP+N-FINDR	12.81°	8.33°	9.83°	10.43°	5.28°	9.34°
SPP+OSP	4.95°	4.16°	9.96°	10.90°	4.62°	6.92°
SPP+VCA	12.42°	4.04°	9.37°	7.87°	6.18°	7.98°
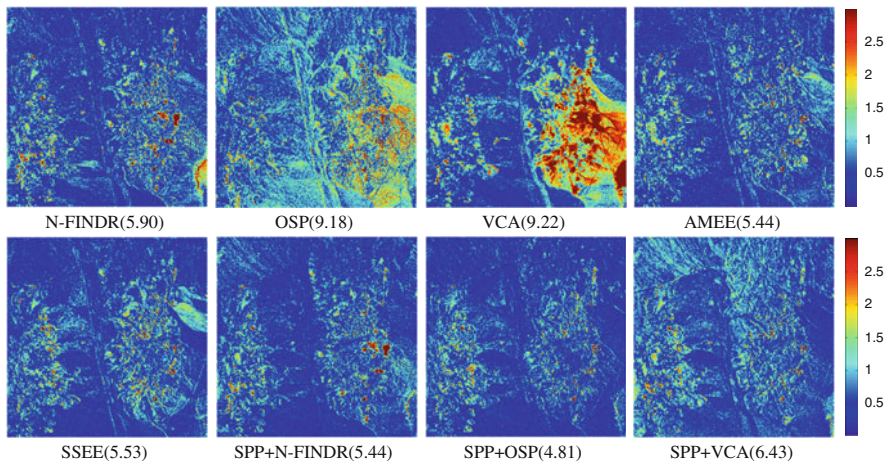
Fig. 12 RMSE reconstruction errors (in percentage) for various endmember extraction algorithms after reconstructing the AVIRIS Cuprite scene

signatures is also reported. In all cases, the number of endmembers to be extracted was set to $p = 14$ after using the VD concept in [10]. Table 1 reveals that the AMEE provides very good results (all SAD scores below 10°), with the SSEE and the SPP+OSP being the algorithms that can provide comparable—but slightly worst—results. Table 1 also reveals that, in this real example, spatial preprocessing generally improves the signature purity of the endmembers extracted by spectral-based algorithms.

On the other hand, Fig. 12 graphically represents the per-pixel root mean square error (RMSE) obtained after reconstructing the AVIRIS Cuprite scene using $p = 14$ endmembers extracted by different methods. It can be seen that the methods using spatial preprocessing (SPP+OSP, SPP+N-FINDR, SPP+VCA) improve their respective spectral-based versions in terms of the quality of image reconstruction, while both AMEE and SSEE also provide lower reconstruction errors than OSP, N-FINDR and VCA. These results suggest the advantages of incorporating spatial information into the automatic extraction of image endmembers from the viewpoint of obtaining more spatially representative spectral signatures which can be used to describe other mixed signatures in the scene.

4.2 Second Experiment: DAIS 7915 and ROSIS Hyperspectral Data

In this section, a set of scenes collected over a so-called *Dehesa* semi-arid ecosystem (formed by *quercus ilex* or cork-oak trees, soil and pasture) is used as a case study to illustrate the applicability of nonlinear neural network-based

unmixing to a real problem. In the Iberian Peninsula, Dehesa systems are used for a combination of livestock, forest and agriculture activity [52]. The outputs of these systems include meat, milk, wool, charcoal, cork bark and grain. Around 12–18% of the area is harvested on a yearly basis. The crops are used for animal feed or for cash cropping, depending on the rainfall of the area. Determination of fractional land-cover using remote sensing techniques may allow for a better monitoring of natural resources in Dehesa agro-ecosystems. Our choice of this type of landscape for evaluating spectral unmixing techniques was made on several accounts. The first one is the availability of hyperspectral image data sets with accurate geo-registration for a real Dehesa test site in Caceres, SW Spain, collected simultaneously in July 2001 by two instruments operating at multiple spatial resolutions: DAIS 7915 and ROSIS, operated by the German Aerospace Agency (DLR). A second major reason is the simplicity of the Dehesa landscape, which greatly facilitates the collection of reliable field data for model validation purposes. It is also important to emphasize that the scenes were collected in summertime, so atmospheric interferers were greatly minimized. Before describing our experiments, we first provide a comprehensive description of the data sets used and ground-truth activities in the study area.

4.2.1 Data Description

The data used in this study consisted of two main components: image data and field measurements of land-cover fractions, collected at the time of image data acquisition. The image data is formed by a ROSIS scene collected at high spatial resolution, with 1.2-m pixels, and its corresponding DAIS 7915 scene, collected at low spatial resolution with 6-m pixels. The spectral range from 504 to 864 nm was selected for experiments, not only because it is adequate for analyzing the spectral properties of the landscape under study, but also because this spectral range is well covered by the two considered sensors through narrow spectral bands. Figure 13 shows the full flightline of the ROSIS scene, which comprises a Dehesa area located between the facilities of University of Extremadura in Cáceres (leftmost part of the flightline) and Guadiloba water reservoir at the center of the flightline. Figure 14a shows the Dehesa test site selected for experiments, which corresponds to a highly representative Dehesa area that contains several cork-oak trees (appearing as dark spots) and several pasture (gray) areas on a bare soil (white) background. Several field techniques were applied to obtain reliable estimates of the fractional land cover for each DAIS 7915 pixel in the considered Dehesa test site:

1. First, the ROSIS image was roughly classified into the three land-cover components above using a maximum-likelihood supervised classification approach based on image-derived spectral endmembers, where Fig. 14b shows the three endmembers used for mapping that were derived using the AMEE algorithm. Our assumption was that the pixels in the ROSIS image were sufficiently small to become spectrally simple to analyze.

Fig. 13 Flightline of a ROSIS hyperspectral scene collected over a Dehesa area in Cáceres, Spain
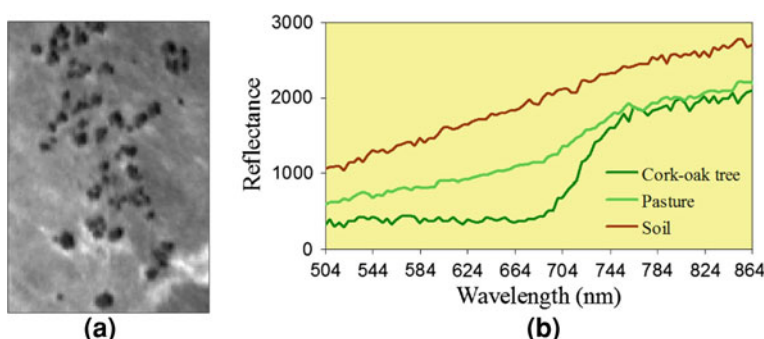
Fig. 14 a Spectral band (584 nm) of a ROSIS Dehesa subset selected for experiments. **b** Endmember signatures of soil, pasture and cork-oak tree extracted by the AMEE algorithm, where scaled reflectance values are multiplied by a constant factor

2. Then, the classified ROSIS image was registered with the DAIS 7915 image using a ground control point-based method with sub-pixel accuracy [53].
3. The classification map was then associated with the DAIS 7915 image to provide an initial estimation of land cover classes for each pixel at the DAIS 7915 image scale. For that purpose, a 6 × 6-m grid was overlaid on the 1.2 × 1.2-m classification map derived from the ROSIS scene, where the geographic coordinates of each pixel center point were used to validate the registration with sub-pixel precision.
4. Next, fractional abundances were calculated within each 6 × 6-m grid as the proportion or ROSIS pixels labeled as cork-oak tree, pasture and soil located within that grid, respectively.
5. Most importantly, the abundance maps at the ROSIS level were thoroughly refined using field measurements (see Fig. 15a) before obtaining the final
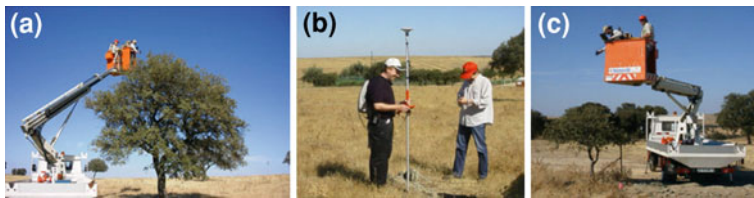
Fig. 15 Ground measurements in the area of study. **a** Spectral sample collection using an ASD FieldSpec Pro spectroradiometer. **b** High-precision GPS geographic delimitation. **c** Field spectral measurements at different altitudes

proportions. Several approaches were developed to refine the initial estimations:

- Fractional land cover data were collected on the ground at more than thirty evenly distributed field sites within the test area. These sites were delineated during the field visit as polygons, using high-precision GPS coordinates (see Fig. 15b).
- Land cover fractions were estimated at each site using a combination of various techniques. For instance, field spectra were collected for several areas using an ASD FieldSpec Pro spectro-radiometer. Of particular interest were field measurements collected on top of tree crowns (Fig. 15c), which allowed us to model different levels of tree crown transparency.
- On the other hand, the early growth stage of pasture during the summer season allowed us to perform ground estimations of pasture abundance in selected sites of known dimensions, using pasture harvest procedures supported by visual inspection and laboratory analyses.

After following the above-mentioned sequence of steps, we obtained a set of approximate fractional abundance labels for each pixel vector in the DAIS 7915 image. Despite our effort to conduct a reliable ground estimation of fractional land-cover in the considered semi-arid environment, absolute accuracy is not claimed. We must emphasize, however, that the combined use of imagery data at different resolutions, sub-pixel ground control-based image registration, and extensive field work including high-precision GPS field work, spectral sample data collection and expert knowledge, represents a novel contribution in the area of spectral mixture analysis validation, in particular, for Dehesa-type ecosystems.

4.2.2 Fractional Abundance Estimation Results

In order to evaluate the accuracy of linear mixture modeling in the considered application, Fig. 16 shows the scatterplots of measured versus FCLSU-estimated fractional abundances for the three considered land-cover materials in the DAIS 7915 (low spatial resolution) image data set, where the diagonal represents perfect match and the two flanking lines represent plus/minus 20% error bound. Here, the
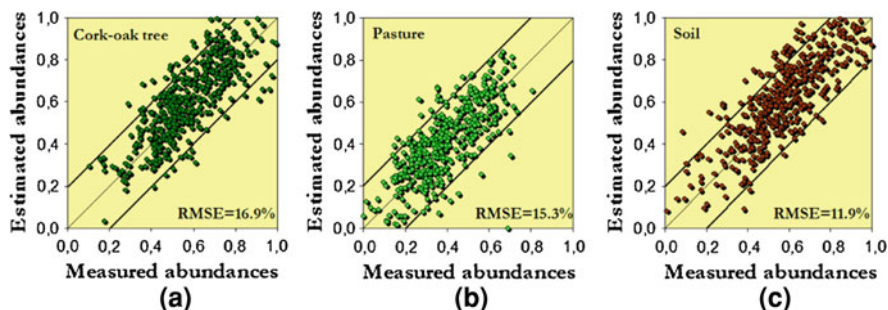
Fig. 16 Abundance estimations of cork-oak tree (**a**), pasture (**b**) and soil (**c**) by the fully constrained linear mixture model from the DAIS 7915 image
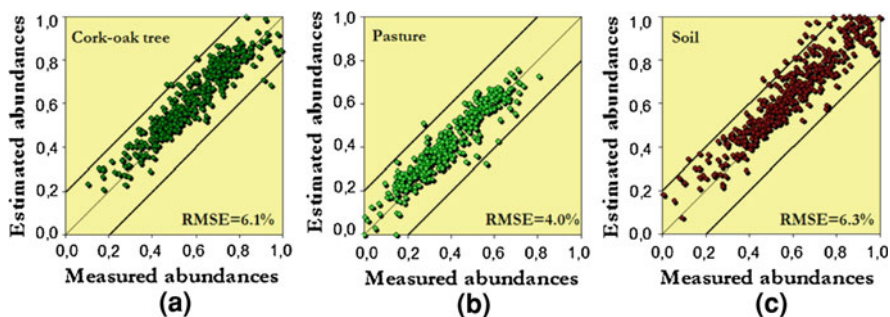
Fig. 17 Abundance estimations of cork-oak tree (**a**), pasture (**b**) and soil (**c**) by the MLP-based mixture model (trained using MTA) from the DAIS 7915 image

three spectral endmembers were derived using the AMEE algorithm, which incorporates spatial information into the endmember extraction process. As expected, the flatness of the test site largely removed topographic influences in the remotely sensed response of soil areas. As a result, most linear predictions for the soil endmember fall within the 20% error bound (see Fig. 16a). On the other hand, the multiple scattering within the pasture and cork-oak tree canopies (and from the underlying surface in the latter case) complicated the spectral mixing in nonlinear fashion, which resulted in a generally higher number of estimations lying outside the error bound, as illustrated in Fig. 16b, c. Also, the RMSE scores in abundance estimation for the soil (11.9%), pasture (15.3%) and cork-oak tree (16.9%) were all above 10% estimation error in percentage, which suggested that linear mixture modeling was not flexible enough to accommodate the full range of spectral variability throughout the landscape.

In order to characterize the Dehesa ecosystem structure better than linear models do, we hypothesized that intelligently selected training data might be required to better characterize nonlinear mixing effects. For this purpose, we applied the MTA algorithm to automatically locate highly descriptive training sites

in the DAIS 7915 scene and then used the obtained samples (and the ground-truth information associated to those samples) to train the proposed MLP-based neural network. Figure 17 shows the scatter plots of measured versus predicted fractional abundances for soil, pasture and cork-oak tree by the proposed MLP-based model, trained with the three endmembers derived by AMEE (see Fig. 14b) plus 40 additional training samples selected by MTA, which represent less than 1% of the total number of pixels in the DAIS 7915 scene. These samples were excluded from the testing set made up of all remaining pixels in the scene. From Fig. 17, it is clear that the utilization of intelligently selected training samples resulted in fewer points outside the two 20% difference lines, most notably, for both pasture and cork-oak abundance estimates. The pattern of the scatter plots obtained for the soil predictions (see Fig. 17a) was similar (in particular, when the soil abundance was high). Most importantly, the RMSE scores in abundance estimation were significantly reduced (with regards to the experiment using FCLSU) for the soil (6.1%), pasture (4%) and cork-oak tree (6.3%). These results confirm our intuition that nonlinear effects in Dehesa landscapes mainly result from multiple scattering effects in vegetation canopies.

Before concluding the chapter it is worth noting that, although abundance sum-to-one and abundance non-negativity constraints were not imposed in our proposed MLP-based learning stage, negative and/or unrealistic abundance estimations (which usually indicate a bad fit of the model and reveal inappropriate endmember/training data selection) were very rarely found in our experiments. Summarizing, the experimental validation carried out in this section indicated that the intelligent incorporation of mixed training samples can enable a more accurate representation of nonlinearly mixed signatures. It was apparent from experimental results that the proposed neural network-based model was able to generate abundance estimates that were close to abundance values measured in the field, using only a few intelligently generated training samples. The need for mixed training data does, however, require detailed knowledge on abundance fractions for the considered training sites. In practice, these data are likely to be derived from imagery acquired at a finer spatial resolution than the imagery to be classified, e.g., using data sets acquired by sensors operating simultaneously at multiple spatial resolutions as it is the case of the DAIS 7915 and ROSIS instruments considered in this experiment. Such multi-resolution studies may also incorporate prior knowledge or ancilliary information, which can be used to help target the location of training sites, and to focus training site selection activities on regions likely to contain the most informative training samples.

5 Parallel Implementation Case Study

The endmember extraction and spectral unmixing techniques introduced in previous sections of this chapter introduce new processing challenges, in particular, for very high-dimensional data sets [54]. From a computational perspective, these

algorithms can be extremely time consuming when applied to real hyperspectral data sets such as the AVIRIS scene in Fig. 11a, with 137 MB in size, or the ROSIS scene in Fig. 13, with about 1 GB of size for the full flightline. At the same time, these techniques exhibit inherent parallelism at multiple levels [55]: across pixel vectors (coarse grained pixel-level parallelism), across spectral information (fine grained spectral-level parallelism), and even across tasks (task-level parallelism). As a result, they map nicely to massively parallel systems such as clusters of computers or heterogeneous networks of workstations [56]. Unfortunately, these systems are expensive and difficult to adapt to on-board data processing scenarios, in which low-weight and low-power integrated components are mandatory to reduce mission payload [57].

An exciting recent development in the field of commodity computing is the emergence of programmable graphics processing units (GPUs) [58, 59], mainly due to the advent of video-game industry. The speed of graphics hardware doubles approximately every six months, which is much faster than the improving rate of the CPU. The ever-growing computational requirements introduced by hyperspectral imaging applications can benefit from this kind of commodity hardware and take advantage of the compact size and relatively low cost of these units, which make them appealing for on-board data processing at much lower costs than those introduced by other hardware devices such as clusters. In the following, we develop a GPU-based implementation of a spectral unmixing chain made up of spatial–spectral endmember extraction using the AMEE algorithm followed by unconstrained linear spectral unmixing (LSU). The chain was implemented using NVidia^{TM} CUDA,[3] a collection of extensions to the C programming language and a runtime library. CUDA's functionality primarily allows a developer to write C functions to be executed on the GPU. CUDA also includes memory management and execution configuration, so that a developer can control the number of GPU processors and threads that are to be invoked during a function's execution. GPU-based algorithms developed in CUDA are constructed by chaining so-called *kernels*, which take one or more streams as inputs and produce one or more streams as outputs.

The first issue that needs to be addressed when porting a hyperspectral imaging algorithm to a GPU is how to map a hyperspectral image onto the GPU memory. Since the size of hyperspectral images usually exceeds the capacity of such memory, we split them into multiple spatial-domain partitions [56] made up of entire pixel vectors (see Fig.18), i.e., each spatial-domain partition incorporates all the spectral information on a localized spatial region and is composed of spatially adjacent pixel vectors. Once the hyperspectral image has been allocated onto the GPU memory, a set of kernels are applied to perform the desired operations. In our case, the kernels needed to implement the AMEE algorithm for endmember extraction followed by LSU for linear spectral unmixing can be summarized as follows:

---

[3] http://www.nvidia.com/object/cuda_home.html
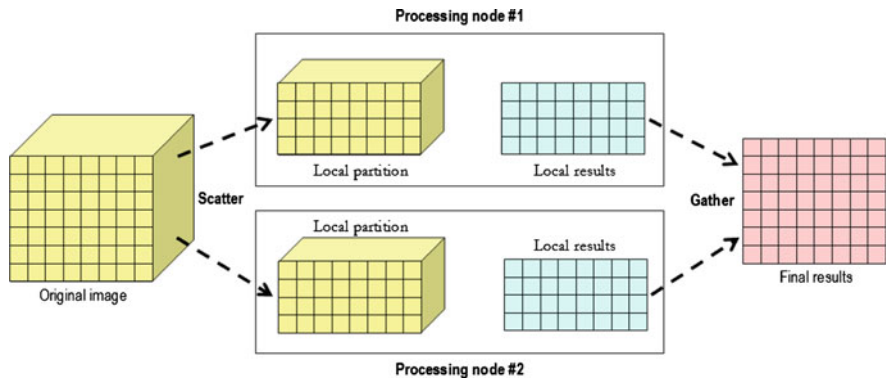
Fig. 18 Spatial-domain decomposition for parallelization of hyperspectral imaging algorithms

- *Cumulative distance*. For each pixel vector, this kernel accumulates the SAD with all the neighboring pixels in order to complete a core operation in the AMEE endmember extraction algorithm. It is based on a single-pass kernel that computes the SAD between two pixel vectors using the inner products and norms produced by the previous kernel. Finally, the kernel calculates, for each pixel vector, the cumulative spectral angle between the pixel and all its neighbors.
- *Max/min finding*. Extended morphological erosion and dilation used by the AMEE algorithm are implemented at this stage through a kernel that applies minimum and maximum reductions. This kernel uses as inputs the cumulative values generated in the previous stage and produces a stream containing (for each pixel) the relative coordinates of the neighboring pixels with maximum and minimum cumulative distance.
- *Eccentricity update*. This kernel updates the morphological eccentricity scores using the maximum/minimum and point-wise distance streams. A complementary kernel applies a threshold to select a set of final AMEE-derived endmembers at the end of the process.
- *Spectral unmixing*. Finally, this kernel uses as inputs the final endmembers selected in the previous stage and produces a set of endmember fractional abundances for each pixel using the unconstrained inversion process in Eq. 2.

The proposed endmember extraction algorithm has been implemented using the Intel C/C++ compiler. The system used in experiments is based on an Intel Core 2 Quad Q6600 CPU running at 2.4 GHz and with 4 GB of RAM. The computer is equipped with an NVidia^{TM} GeForce 8800 GTX with 16 multiprocessors, each composed of eight SIMD processors operating at 1,350 Mhz. Each multiprocessor has 8,192 registers, a 16 KB parallel data cache of fast shared memory, and access to 768 MB of global memory. The GPU architecture is graphically illustrated in Fig. 19. The hyperspectral data set used in our experiments is the AVIRIS Cuprite scene.
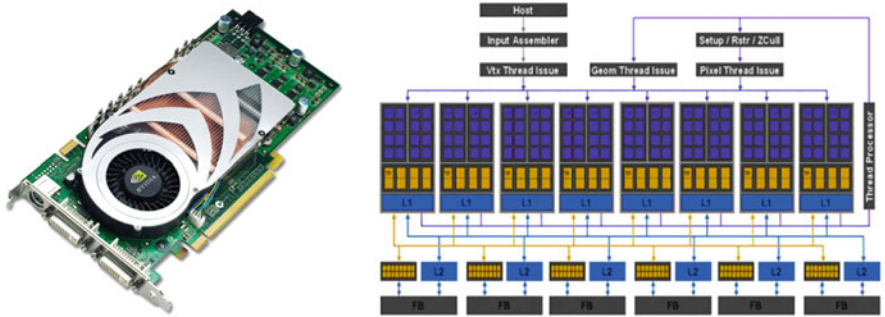
Fig. 19 Architecture of the NVidia^{TM} GeForce 8800 GTX graphics card used in experiments

Table 2 Processing time (seconds) and speedups for the dual-core CPU and GPU implementations

Algorithm	Processing time (CPU)	Processing time (GPU)	Speedup
AMEE	42.797	1.678	25.504
LSU	4.953	1.297	3.818

Table 2 shows the execution times and speedups measured for the GPU-based implementations of the AMEE and unconstrained LSU algorithms compared to their execution in the quad-core CPU of the system in which the GPU was integrated. The speedup achieved by the GPU implementation of the AMEE algorithm over its respective CPU implementations is close to 25. It should be noted that the speedup achieved for the GPU implementation of AMEE was independent of the structuring element size (the results displayed in Table 2 correspond to a structuring element of 5×5 pixels in size which appropriate for endmember extraction from the AVIRIS Cuprite scene, but similar speedups were achieved with other structuring element sizes). On the other hand, Table 2 indicates that the speedup achieved for the parallel implementation of the LSU stage was lower. This is mainly due to the fact that the serial version of LSU is only takes around 5 s to be completed in the quad-core CPU, and it is more difficult to achieve significant speedups in this case since the communication time needed to transfer the data from the CPU to the GPU is more relevant in this case when compared to the total time to finalize the computations in the GPU. As a result, the ratio of computations to communications is smaller for the parallel version of LSU than for the parallel version of AMEE, which has an effect on the achieved speedup. Despite these observations, it can be seen from Table 2 that the considered AVIRIS data cube could be processed in parallel by a full unmixing chain made up of spatial–spectral endmember extraction followed by linear spectral unmixing in just 2.975 s. This response is not strictly in real-time since the cross-track line scan time in AVIRIS, a push-broom instrument, is quite fast (8.3 ms to collect 512 full pixel vectors), which introduces the need to process the considered scene (350×350 pixels) in 1.985 s to fully achieve real-time performance. However, we believe that the achieved (near) real-time response time would be relevant in many application domains. Further developments will be

pursued in future work in order to approximate real-time performance for on-board data exploitation.

6 Conclusions and Future Research

Endmember extraction is the process of selecting a collection of pure signature spectra of the materials present in a remotely sensed hyperspectral scene. These pure signatures are then used to decompose the scene into abundance fractions by means of a spectral unmixing algorithm. Most techniques available in the endmember extraction literature rely on exploiting the spectral properties of the data alone. As a result, the search for endmembers in a scene is conducted by treating the data as a collection of spectral measurements with no spatial arrangement. In this chapter, we have discussed the role of spatial information in the search for spectral endmembers and further demonstrated via experimental results, using AVIRIS hyperspectral data collected in the framework of a mineral mapping application, that the linear mixture model can benefit from the integration of spatial and spectral information in the task of selecting endmembers. An investigation on the use of the considered spatial–spectral endmember extraction algorithms in conjunction with source separation techniques, such as those described in [60], is a topic deserving future research in this context.

When complex mixtures are present in hyperspectral scenes, nonlinear mixture models may best characterize the resultant mixed spectra for certain endmember distributions. In order to address this issue, we have developed a nonlinear, neural network-based mixture model which is initialized using linear spectral unmixing concepts. The proposed approach is trained with highly representative training sets which can accurately explain the complex nature of the data using only a few training samples. Our study reveals that the most informative training samples for nonlinear mixture characterization are the most highly mixed signatures in the input data set. This observation is in contrast with the overall approach in linear spectral unmixing in which only the purest spectral signatures are used to characterize and decompose spectral mixtures. Critically, if the regions expected to contain the most highly informative training samples for spectral mixture modeling can be identified in advance, then it is possible to direct the training data acquisition procedures to these regions, and thus reduce the number of required training sites without loss of prediction accuracy. This issue is of particular importance in real applications based on the use of airborne/satellite images, in which the acquisition of large training sets is generally very costly in terms of time and finance. To illustrate the concepts above, we have conducted experiments using a set of real hyperspectral images, collected at different altitudes by the DAIS 7915 and ROSIS imaging spectrometers in the framework of an agriculture and farming application in the region of Extremadura, Spain. Although the reported results are promising, it would be also useful to explore in future work the behaviour of spatial–spectral methods in cases where the linear mixture model

assumption is no longer valid to describe the mixing systematics of the observed materials, thus conducting a more detailed evaluation of linear versus nonlinear mixture models in different application domains.

Finally, in order to address the extremely high computational requirements introduced by endmember extraction and spectral unmixing applications, this chapter has also presented a parallel implementation case study in which an unmixing chain made up of spatial–spectral endmember extraction followed by unconstrained linear spectral unmixing has been implemented on a specialized graphics processor (GPU). Our experimental results indicate that a low-weight and low-power specialized hardware device such as a GPU has the potential to bridge the gap towards real-time analysis of high dimensional data. This kind of specialized, on-board processing devices are essential to reduce mission payload and obtain analysis results quickly enough for practical use in real applications. Further experimentation will additional hyperspectral scenes will be pursued in future work in order to approximate real-time performance of endmember extraction and spectral unmixing applications for on-board data exploitation.

References

1. Goetz, A.F.H., Vane, G., Solomon, J.E., Rock, B.N.: Imaging spectrometry for earth remote sensing. Science **228**, 1147–1153 (1985)
2. Plaza, A., Benediktsson, J.A., Boardman, J., Brazile, J., Bruzzone, L., Camps-Valls, G., Chanussot, J., Fauvel, M., Gamba, P., Gualtieri, J., Marconcini, M., Tilton, J.C., Trianni, G.: Recent advances in techniques for hyperspectral image processing. Remote Sens. Environ. **113**, 110–122 (2009)
3. Schaepman, M.E., Ustin, S.L., Plaza, A., Painter, T.H., Verrelst, J., Liang, S.: Earth system science related imaging spectroscopy—an assessment. Remote Sens. Environ. **113**, 123–137 (2009)
4. Adams, J.B., Smith, M.O., Johnson, P.E.: Spectral mixture modeling: a new analysis of rock and soil types at the Viking Lander 1 site. J. Geophys. Res. **91**, 8098–8112 (1986)
5. Keshava, N., Mustard, J.F.: Spectral unmixing. IEEE Signal Process. Mag. **19**(1), 44–57 (2002)

6. Green, R.O., Eastwood, M.L., Sarture, C.M., Chrien, T.G., Aronsson, M., Chippendale, B.J., Faust, J.A., Pavri, B.E., Chovit, C.J., Solis, M., et al.: Imaging spectroscopy and the airborne visible/infrared imaging spectrometer (AVIRIS). Remote Sens. Environ. **65**(3), 227–248 (1998)

7. Ball, J.E., Bruce, L.M., Younan, N.: Hyperspectral pixel unmixing via spectral band selection and dc-insensitive singular value decomposition. IEEE Geosci. Remote Sens. Lett. **4**(3), 382–386 (2007)

8. Heinz, D., Chang, C.-I.: Fully constrained least squares linear mixture analysis for material quantification in hyperspectral imagery. IEEE Trans. Geosci. Remote Sens. **39**, 529–545 (2001)

9. Plaza, A., Martinez, P., Perez, R., Plaza, J.: A quantitative and comparative analysis of endmember extraction algorithms from hyperspectral data. IEEE Trans. Geosci. Remote Sens. **42**(3), 650–663 (2004)

10. Chang, C.-I.: Hyperspectral Imaging: Techniques for Spectral Detection and Classification. Kluwer Academic Publishers, New York (2003)

11. Guilfoyle, K.J., Althouse, M.L., Chang, C.-I.: A quantitative and comparative analysis of linear and nonlinear spectral mixture models using radial basis function neural networks. IEEE Trans. Geosci. Remote Sens. **39**, 2314–2318 (2001)

12. Plaza, J., Plaza, A., Perez, R., Martinez, P.: On the use of small training sets for neural network-based characterization of mixed pixels in remotely sensed hyperspectral images. Pattern Recognit. **42**, 3032–3045 (2009)

13. Harsanyi, J.C., Farrand, W., Chang, C.-I.: Detection of subpixel spectral signatures in hyperspectral image sequences. Proc. American Society on Photogrammetry and Remote Sensing Annual Meeting, pp. 236–247 (1994).

14. Boardman, J.W., Kruse, F.A., Green, R.O.: Mapping target signatures via partial unmixing of AVIRIS data. In: Proceedings of JPL Airborne Earth Science Workshop, pp. 23–26 (1995)

15. Winter, M.E.: N-FINDR: an algorithm for fast autonomous spectral endmember determination in hyperspectral data. Proc. SPIE **3753**, 266–277 (1999)

16. Winter, M.E.: A proof of the N-FINDR algorithm for the automated detection of endmembers in a hyperspectral image. Proc. SPIE Algorithms Technol. Multispectral Hyperspectral Ultraspectral Imagery X **5425**, 31–41 (2004)

17. Zortea, M., Plaza, A.: A quantitative and comparative analysis of different implementations of N-FINDR: a fast endmember extraction algorithm. IEEE Geosci. Remote Sens. Lett. **6**, 787–791 (2009)

18. Neville, R.A., Staenz, K., Szeredi, T., Lefebvre, J., Hauff, P.: Automatic endmember extraction from hyperspectral data for mineral exploration. In: Proceedings of 21st Canadian Symposium Remote Sensing, pp. 21–24 (1999)

19. Bowles, J.H., Palmadesso, P.J., Antoniades, J.A., Baumback, M.M., Rickard, L.J.: Use of filter vectors in hyperspectral data analysis. Proc. SPIE Infrared Spaceborne Remote Sens. III **2553**, 148–157 (1995)

20. Ifarraguerri, A., Chang, C.-I.: Multispectral and hyperspectral image analysis with convex cones. IEEE Trans. Geosci. Remote Sens. **37**(2), 756–770 (1999)

21. Nascimento, J.M.P., Bioucas-Dias, J.M.: Vertex component analysis: a fast algorithm to unmix hyperspectral data. IEEE Trans. Geosci. Remote Sens. **43**(4), 898–910 (2005)

22. Harsanyi, J.C., Chang, C.-I.: Hyperspectral image classification and dimensionality reduction: an orthogonal subspace projection. IEEE Trans. Geosci. Remote Sens. **32**(4), 779–785 (1994)

23. Berman, M., Kiiveri, H., Lagerstrom, R., Ernst, A., Dunne, R., Huntington, J.F.: ICE: a statistical approach to identifying endmembers in hyperspectral images. IEEE Trans. Geosci. Remote Sens. **42**(10), 2085–2095 (2004)

24. Miao, L., Qi, H.: Endmember extraction from highly mixed data using minimum volume constrained nonnegative matrix factorization. IEEE Trans. Geosci. Remote Sens. **45**(3), 765–777 (2007)

25. Chang, C.-I., Wu, C.-C., Liu, W., Ouyang, Y.-C.: A new growing method for simplex-based endmember extraction algorithm. IEEE Trans. Geosci. Remote Sens. **44**(10), 2804–2819 (2006)

26. Wang, J., Chang, C.-I.: Applications of independent component analysis in endmember extraction and abundance quantification for hyperspectral imagery. IEEE Trans. Geosci. Remote Sens. **44**(9), 2601–2616 (2006)

27. Plaza, A., Chang, C.-I.: Impact of initialization on design of endmember extraction algorithms. IEEE Trans. Geosci. Remote Sens. **44**(11), 3397–3407 (2006)

28. Chang, C.-I., Plaza, A.: A fast iterative algorithm for implementation of pixel purity index. IEEE Geosci. Remote Sens. Lett. **3**(1), 63–67 (2006)

29. Zare, A., Gader, P.: Hyperspectral band selection and endmember detection using sparsity promoting priors. IEEE Geosci. Remote Sens. Lett. **5**(2), 256–260 (2008)

30. Plaza, A., Martinez, P., Plaza, J., Perez, R.: Dimensionality reduction and classification of hyperspectral image data using sequences of extended morphological transformations. IEEE Trans. Geosci. Remote Sens. **43**(3), 466–479 (2005)

31. Plaza, A., Martinez, P., Perez, R., Plaza, J.: Spatial/spectral endmember extraction by multidimensional morphological operations. IEEE Trans. Geosci. Remote Sens. **40**(9), 2025–2041 (2002)

32. Rogge, D.M., Rivard, B., Zhang, J., Sanchez, A., Harris, J., Feng, J.: Integration of spatial–spectral information for the improved extraction of endmembers. Remote Sens. Environ. **110**(3), 287–303 (2007)

33. Zortea, M., Plaza, A.: Spatial preprocessing for endmember extraction. IEEE Trans. Geosci. Remote Sens. **47**, 2679–2693 (2009)

34. Chang, C.-I.: Hyperspectral Data Exploitation: Theory and Applications. Wiley, New York (2007)

35. Richards, J.A., Jia, X.: Remote Sensing Digital Image Analysis: An Introduction. Springer, Berlin (2006)

36. Landgrebe, D.A.: Signal Theory Methods in Multispectral Remote Sensing. Wiley, New York (2003)

37. Green, A.A., Berman, M., Switzer, P., Craig, M.D.: A transformation for ordering multispectral data in terms of image quality with implications for noise removal. IEEE Trans. Geosci. Remote Sens. **26**, 65–74 (1988)

38. Ren, H., Chang, C.-I.: Automatic spectral target recognition in hyperspectral imagery. IEEE Trans. Aerosp. Electron. Syst. **39**(4), 1232–1249 (2003)

39. Chang, C.-I., Heinz, D.: Constrained subpixel target detection for remotely sensed imagery. IEEE Trans. Geosci. Remote Sens. **38**, 1144–1159 (2000)

40. Bishop, C.M.: Neural Networks for Pattern Recognition. Oxford University Press, Oxford (1995)

41. Baraldi, A., Binaghi, E., Blonda, P., Brivio, P.A., Rampini, P.: Comparison of the multilayer perceptron with neuro-fuzzy techniques in the estimation of cover class mixture in remotely sensed data. IEEE Trans. Geosci. Remote Sens. **39**, 994–1005 (2001)

42. Plaza, J., Plaza, A.: Spectral mixture analysis of hyperspectral scenes using intelligently selected training samples. IEEE Geosci. Remote Sens. Lett. **7**, 371–375 (2010)

43. Liu, W., Wu, E.Y.: Comparison of non-linear mixture models. Remote Sens. Environ. **18**, 1976–2003 (2004)

44. Zhuang, X., Engel, B.A., Lozano, D.F., Fernßndez, R.B., Johannsen, C.J.: Optimization of training data required for neuro-classification. Int. J. Remote Sens. **15**, 3271–3277 (1999)

45. Prasad, S., Bruce, L.M.: Overcoming the small sample size problem in hyperspectral classification and detection tasks. Proc. IEEE Int. Geosci. Remote Sens. Symp. **5**, 381–384 (2008)

46. Chi, M., Bruzzone, L.: A semilabeled-sample-driven bagging technique for ill-posed classification problems. IEEE Geosci. Remote Sens. Lett. **2**, 69–73 (2005)

47. Foody, G.M.: The significance of border training patterns in classification by a feedforward neural network using backpropagation learning. Int. J. Remote Sens. **20**, 3549–3562 (1999)

48. Plaza, J., Plaza, A., Martinez, P., Perez, R.: Nonlinear mixture models for analyzing laboratory simulated-forest hyperspectral data. Proc. SPIE **5508**, 660–670 (2003)
49. Borel, C.C., Gerslt, S.A.W.: Nonlinear spectral mixing models for vegetative and soil surfaces. Remote Sens. Environ. **47**, 403–416 (1994)
50. Clark, R.N., Swayze, G.A., Livo, K.E., Kokaly, R.F., Sutley, S.J., Dalton, J.B., McDougal, R.R., Gent, C.A.: Imaging spectroscopy: earth and planetary remote sensing with the USGS tetracorder and expert systems. J. Geophys. Res. **108**, 1–44 (2003)
51. Swayze, G., Clark, R.N., Kruse, F., Sutley, S., Gallagher, A.: Ground-truthing AVIRIS mineral mapping at Cuprite, Nevada. In: Proceedings of JPL Airborne Earth Science Workshop, pp. 47–49 (1992)
52. Pulido, F.J., Diaz, M., Hidalgo, S.J.: Size structure and regeneration of spanish holm oak quercus ilex forests and dehesas: effects of agroforestry use on their long-term sustainability. For. Ecol. Manage. **146**, 1–13 (2001)
53. Plaza, A., Moigne, J.L., Netanyahu, N.S.: Morphological feature extraction for automatic registration of multispectral scenes. Proc. IEEE Int. Geosci. Remote Sens. Symp. **1**, 421–424 (2007)
54. Plaza, A., Chang, C.-I.: High Performance Computing in Remote Sensing. CRC Press, Boca Raton (2007)
55. Plaza, A., Plaza, J., Valencia, D.: Impact of platform heterogeneity on the design of parallel algorithms for morphological processing of high-dimensional image data. J. Supercomput. **40**, 81–107 (2007)
56. Plaza, A., Valencia, D., Plaza, J., Martinez, P.: Commodity cluster-based parallel processing of hyperspectral Imagery. J. Parallel Distrib. Comput. **66**(3), 345–358 (2006)
57. Plaza, A., Chang, C.-I.: Clusters versus FPGA for parallel processing of hyperspectral imagery. Int. J. High Perform. Comput. Appl. **22**(4), 366–385 (2008)
58. Setoain, J., Prieto, M., Tenllado, C., Plaza, A., Tirado, F.: Parallel morphological endmember extraction using commodity graphics hardware. IEEE Geosci. Remote Sens. Lett. **43**, 441–445 (2007)
59. Tarabalka, Y., Haavardsholm, T.V., Kasen, I., Skauli, T.: Real-time anomaly detection in hyperspectral images using multivariate normal mixture models and GPU processing. J. Real-Time Image Process. **4**, 1–14 (2009)
60. Moussaoui, S., Hauksdottir, H., Schmidt, F., Jutten, C., Chanussot, J., Brie, D., Doute, S., Benediktsson, J.: On the decomposition of Mars hyperspectral data by ICA and Bayesian positive source separation. Neurocomputing **71**, 2194–2208 (2008)